Physics in Medicine &
Biology

Evaluation of radiological properties and anisotropy with air channels analysis in 3D-printed flexible lung-mimicking materials for radiotherapy

To cite this article: Roua Abdulrahim *et al* 2026 *Phys. Med. Biol.* **71** 055016

IOP Publishing *Phys. Med. Biol.* **71** (2026) 055016 https://doi.org/10.1088/1361-6560/ae456d

Physics in Medicine & Biology

IPEM
Institute of Physics and Engineering in Medicine

RECEIVED
21 November 2025

REVISED
29 January 2026

ACCEPTED FOR PUBLICATION
12 February 2026

PUBLISHED
13 March 2026

PAPER

Evaluation of radiological properties and anisotropy with air channels analysis in 3D-printed flexible lung-mimicking materials for radiotherapy

Roua Abdulrahim[1,2,*], **Didier Lustermans**[1], **Murillo Bellezzo**[1], **Behzad Rezaeifar**[1], **Brigitte Reniers**[2,3], **Frank Verhaegen**[1,3] **and Gabriel Paiva Fonseca**[1,3,*]

[1] Department of Radiation Oncology (Maastro), GROW Research Institute for Oncology and Reproduction, Maastricht University Medical Centre+, Maastricht, The Netherlands
[2] Research group NuTeC, Centre for Environmental Sciences, Hasselt University, Diepenbeek, Belgium
[3] The senior authors contributed equally.
[*] Authors to whom any correspondence should be addressed.

E-mail: roua.abdulrahim@maastro.nl and gabriel.paivafonseca@maastro.nl

Keywords: 3D-printing, radiotherapy QA, lung-mimicking flexible materials, anisotropy, air-channels

Supplementary material for this article is available online

Abstract

Objective. Three-dimensional (3D) printing is increasingly used for radiotherapy quality assurance (QA) phantoms, yet, reproducing the structural heterogeneity and radiological properties of lung tissue remains challenging. This study evaluates thermoplastic polyurethane (TPU) for dynamic lung-mimicking phantoms, selected for its flexibility while preserving print-defined geometry, with a focus on radiological equivalence, directional anisotropy, and the detectability of sub-millimetre air channels. *Approach.* Eleven TPU materials with various colours and Shore hardness (63–82) were printed into gyroid-patterned inserts of varying infill densities. Effective atomic number (Z_{eff}) and relative electron density (RED) were determined using dual-energy computed tomography (CT). Anisotropy and internal air channels were assessed in five orientations using micro-CT, clinical CT, and flat-panel detector (FPD) imaging, and compared to a voxelised digital model derived from G-code toolpaths. *Main results.* Measured Z_{eff} ranged from 6.3 ± 0.6 to 11.1 ± 0.2, with pigment-driven variation up to 66% within identical material categories. Seven materials achieved lung mimicking Z_{eff} (around 7.55). RED increased with infill and mimicked lung references (0.28–0.43) at moderate infill. The low-infill insert contained 0.7 mm air channels visible in all modalities. The high-infill insert contained 0.3 mm channels, resolved accurately by the micro-CT and FPD but not reliably resolved by clinical CT due to resolution limitations. The digital model indicated diagonal anisotropy, micro-CT and FPD indicated near-isotropy in low and high infill, while CT showed apparent anisotropy due to its resolution limitations. *Significance.* TPU-based gyroid phantoms are suitable lung-mimicking candidates for radiotherapy QA of imaging and dosimetry. Their periodic air-channels are reliably resolved by high-resolution imaging (micro-CT or FPD), but may be distorted by clinical CT, particularly in resolution-limited orientations, the digital model supports pre-print evaluation of these air-channels. Because undetected internal heterogeneities may affect dose calculation accuracy, high-resolution imaging when available, is preferred for assessing the internal structure of 3D-printed phantoms.

1. Introduction

Effective quality assurance (QA) in radiotherapy is supported by phantoms that reproduce patient anatomy and motion. There are several commercial thorax phantoms built from solid homogeneous structures made of water or tissue-mimicking materials. These phantoms have contributed greatly to QA. However, they do not capture fine anatomical features of the human lung, such as the bronchi or lung tissue density variations (Schiefer *et al* 2010, Hurkmans *et al* 2011, Subramanian *et al* 2015, Öllers *et al* 2020). Some thorax phantoms can simulate realistic respiration motion and offer clinically valuable functionality for QA (Tanyi *et al* 2007, Saito *et al* 2023). However, they are limited by high cost, restricted customisability, and simplified modelling of tissue heterogeneity (Dunn *et al* 2012, Craft and Howell 2017, Sevillano *et al* 2020).

These gaps have been addressed by means of three-dimensional (3D) printing. In this, fused deposition modelling (FDM) is applied to create patient-specific thorax replicas with detailed internal anatomy at relatively low cost (Hernandez-Giron *et al* 2019, Kunert *et al* 2023). These developments allow the creation of customised structures, with FDM offering greater geometric control than traditional methods, such as casting and moulds (Chacón *et al* 2017, Hohimer *et al* 2017, Gebisa and Lemu 2018, Garg *et al* 2022, Martín-Sosa *et al* 2025). By tuning 3D printing parameters, printed samples have achieved lung-mimicking computed tomography (CT) numbers (Dancewicz *et al* 2017, McGarry *et al* 2020, Tino *et al* 2022). Although this matching is useful, CT numbers alone may be misleading. Materials containing elements with high atomic numbers, such as copper or iron, can produce bone-like CT numbers despite their lower physical density (Fonseca *et al* 2023). To characterise the composition more accurately, the effective atomic number (Z_{eff}) and relative electron density (RED) can be assessed, particularly for dosimetry applications.

In previous work on heterogeneous adult thorax phantoms, lung tissue is mimicked using rigid thermoplastics, such as polylactic acid (PLA) and acrylonitrile butadiene styrene (ABS). Bustillo *et al* used PLA printed at 20% infill to mimic lung tissue, reporting a RED of 0.203. Hatamikia *et al* reported that PLA printed at 30% infill achieved lung-mimicking CT numbers of -482 ± 45 HU. However, these materials are inherently rigid and are therefore limited to static phantom designs. Other studies such as Bakhtiari Moghaddam *et al* use silicones, which provide high flexibility, but rely on casting rather than standard 3D-printing, which limits control over the internal geometry (Bustillo *et al* 2019, Hatamikia *et al* 2022, Bakhtiari Moghaddam *et al* 2025).

In contrast, thermoplastic polyurethane (TPU) is an elastomer that exhibits rubber-like elastic deformation, enabling compression while maintaining its structural integrity (Lee *et al* 2019, León-Calero *et al* 2021, Holmes *et al* 2022). A study on deformable lung phantoms, has shown that 3D-printed TPU can reproduce lung-mimicking CT numbers while still remaining sufficiently flexible to undergo breathing-like deformation (Im *et al* 2025). These considerations motivated the selection of TPU as the material evaluated in this study.

A recent study by Lustermans *et al* (2024) presented a dynamic anthropomorphic lung phantom with internal anatomy (bronchi and tumours). The lung was 3D-printed using TPU, whose Z_{eff} was measured at (10.1 ± 0.3), notably higher than the lung parenchyma reference value of 7.55 (White *et al* 1989). This finding indicates that an alternative TPU filament with a lower Z_{eff} must be explored for the application of phantoms in dosimetry. A factor that has been shown to influence the Z_{eff} of materials is pigmentation, but has not been investigated in TPU materials (Solc *et al* 2018, Ma *et al* 2021, Fonseca *et al* 2023).

To mimic human lung tissue, phantoms are 3D-printed using low infill densities, which increases the air-to-material volume ratio. Depending on the pattern, it may create air gaps that span the full depth of the phantom in certain orientations, forming air channels, which do not exist in real lungs. These channels may distort dose measurements; therefore, their frequency and size must be quantified to prevent dose measurement bias (Madamesila *et al* 2016).

Another important consideration is the anisotropy of a 3D-printed phantom, based on its pattern and material distribution, which may affect performance in radiotherapy QA. In complex radiotherapy treatments involving multiple beam angles, anisotropic features within the phantom can lead to orientation-dependent differences in attenuation and dose deposition, depending on the irradiation angle. Previous imaging studies have reported that gyroid infill patterns can reduce orientation-dependent variations in CT numbers compared with other infill patterns. However, this apparent isotropy depends on the 3D-printing parameters and the spatial resolution of the imaging system used (Tino *et al* 2019, Fonseca *et al* 2023, Bustillo *et al* 2025). The suitability of low-infill gyroid structures for accurately representing both imaging and dosimetric properties remains incompletely characterised and warrants further investigation. This is particularly relevant because standard clinical CT may not resolve fine features such as air channels, potentially leading to discrepancies between the true dose delivered and the dose calculated by the treatment planning system, assuming a homogeneous volume as acquired by the CT.

In this study, commercially available flexible filaments are evaluated as lung-mimicking materials, focusing on their radiological properties such as Z_{eff} and RED, anisotropy in imaging response, and air-channel formation when printing in low and high infill gyroid structures. Multiple imaging modalities are used to assess anisotropy and the presence of air channels; a clinical CT, a micro-CT, and a flat panel detector are used and benchmarked against a voxelised digital model to determine the reliability of each system in resolving internal structures. The goal is to guide the design, manufacturing, and verification of isotropic dynamic lung phantoms for radiotherapy QA.

2. Materials and methods

To characterise the radiological properties and anisotropy of flexible 3D printing materials, the workflow in figure 1 was used.

2.1. Radiological and physical properties evaluation

2.1.1. 3D printing of cylindrical inserts

Inserts were manufactured using the Filaflex TPU filament (Recreus Industries, Spain) in a direct-drive 3D printer (Creality Ender-3 S1, Shenzhen Creality 3D Technology, China). TPU was chosen for its flexibility, which allows compression of printed objects and can simulate respiratory motion in phantom applications. The elemental composition ($C_{19}H_{26}N_2O_4$) was reported by León-Calero *et al*(2021) using NMR spectroscopy. This formulation was characterised for a single hardness grade and does not account for variations in different colours or manufacturer-specific formulations. TPU is generally composed of soft, flexible polymer chains covalently linked with harder urethane segments, with the exact chemical balance tailored by manufacturers to tune mechanical properties.

Shore hardness (a scale, 0–100) quantifies resistance to indentation, lower values indicate softer materials, while higher values indicate a stiffer material. The filaments used in this study exhibited Shore hardness values ranging from 63 A to 82 A (table 1).

The cylindrical inserts were designed using Fusion 360 (Autodesk Inc., USA) and then sliced using IdeaMaker 3D slicing software (RAISE 3D Technologies Inc., USA). Prior to printing, the TPU filaments were dried for 24 h at 55 °C to reduce moisture using a heated filament dryer (FilaDryer S2, SunLu Industrial, China).

The 3D-printing settings are given in table 2. They were initially selected based on the manufacturer's recommendations and later optimised through material characterisation. A reduced nozzle diameter (0.25 mm) was adopted, as it resulted in increased CT homogeneity. Final parameters were selected based on print consistency, dimensional accuracy, and CT homogeneity, quantified by the standard deviation of CT numbers.

2.1.2. Evaluation of effective atomic number and RED

A cylindrical insert with variable infill density was 3D-printed to characterise the Z_{eff} and RED of the TPU materials (figure 2). The insert consisted of five stacked segments, each 10 mm in height, with infill densities of 100%, 60%, 30%, 20%, and 10%. This design enabled evaluation of both fully dense material properties and the range of RED values achievable through infill modification.

A quantitative evaluation of Z_{eff} and RED was performed following the dual-energy CT (DECT) methodology described by Hünemohr *et al* (2014) and Lustermans *et al* (2025). Scans were acquired on a SOMATOM Confidence CT scanner (Siemens Healthineers, Germany) and analysed using the open-source software AMIGOpy (www.amigo-medphys.com). Calibration was performed using the Gammex Advanced Electron Density Phantom (Model 1467, Sun Nuclear—a Mirion Medical Company, USA), utilising its tissue-mimicking inserts, which include lung, adipose, soft tissue, and multiple bone compositions. Scans were acquired at low and high x-ray energies (80 and 140 kVp) and calibration constants were determined by applying a least-squares fit to the CT numbers of the tissue-mimicking inserts.

RED was calculated as a weighted combination of low and high energy CT numbers, while Z_{eff} was obtained from the non-linear relationship between x-ray attenuation and atomic composition. The equations are based on Hünemohr *et al* (2014) and implemented in the software AMIGOpy, as detailed by Lustermans *et al* (2025). A Mayneord exponent of $m = 3.1$ was used in the Z_{eff} calculation as recommended by Hünemohr *et al* (2014) for materials with atomic numbers below iodine.

After completion of the calibration, the 3D-printed TPU inserts were placed within the same Gammex phantom to ensure identical imaging conditions. Inserts were placed in the head-sized section of the phantom and scanned in one acquisition, shown in the supplementary materials. DECT scans (80/140 kVp tube voltages, a slice thickness of 1 mm, a field-of-view 300 mm, a spiral pitch factor of 0.35, the reconstruction kernel Qr40s/3, and a CTDIvol (32 cm) of 40 mGy) were acquired using the same CT scanner as the calibration. Z_{eff} and RED values of the 3D-printed inserts were plotted against standard lung tissue-mimicking materials.

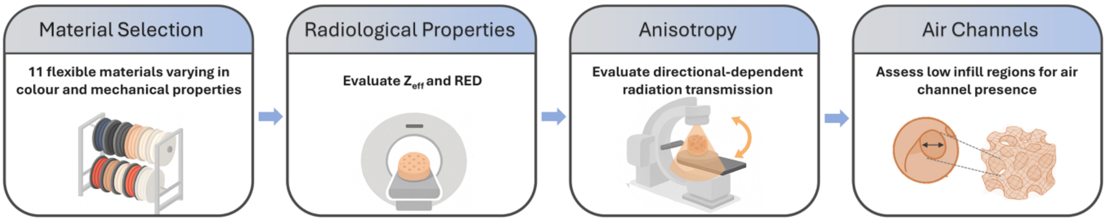

Figure 1. A summary of the evaluations done in this study, using eleven TPU materials. The 3D-printed inserts are assessed using quantitative dual-energy CT imaging to characterise their radiological properties. The anisotropy and air channels are assessed using a digital model, a micro-CT, a clinical CT, and a flat-panel detector.

Table 1. List of flexible materials evaluated.

Filament name	ID	Shore hardness	Colour[a]
Filaflex 60 A PRO[b]	63White	63 A	White
	63Black	63 A	Black
	63Skin	63 A	Nude
Filaflex 70 A Ultra-Soft	70Red	70 A	Red
	70Black	70 A	Black
	70Navy	70 A	Navy
	70Clear	70 A	Clear
Filaflex Foamy	78Natural	78 A	Natural
	78Black	78 A	Black
Filaflex 82 A	82Skin	82 A	Nude
	82Red	82 A	Red

[a] Colour names are as defined by the manufacturer.

[b] The Filaflex 60 A 'PRO' has a measured Shore hardness of 63 A according to the manufacturer's technical datasheet, despite the filament name indicating 60 A.

Table 2. 3D printing settings used in manufacturing the cylindrical inserts.

3D printing settings	Variable density cylinder
Printing temperature (°C)	240
Infill density (%)	100, 60, 30, 20, 10
Flow (%)	136
Nozzle diameter (mm)	0.25
Layer height (mm)	0.18
Line width (mm)	0.24
Infill pattern	Gyroid
Speed (mm s^{-1})	22.5

2.2. Anisotropy evaluation

In this study, anisotropy is defined as orientation-dependent variation in the internal infill distribution, quantified through imaging-derived attenuation and air-channel characteristics (size and frequency). This variation is relevant for radiotherapy QA, where dose delivery from multiple beam angles is common practice, and assumes uniform attenuation through a homogeneous phantom.

The inserts were printed using the gyroid infill pattern, a 3D periodic lattice. At low infill densities used to mimic lung tissue, air gaps within each printed layer become larger, and upon layer stacking, these gaps can align to form continuous hollow air channels extending through the depth of the structure. These air channels may perturb radiation beam propagation and thereby affect dose delivery in 3D-printed phantoms.

To evaluate directional uniformity and air channel formation, CT and micro-CT scans were performed on the inserts and compared to an idealised digital model generated by voxelising the print geometry. Complementary two-dimensional (2D) transmission measurements were acquired using a flat-panel detector (FPD). While the FPD was not calibrated for dosimetry, it provided a sensitive method

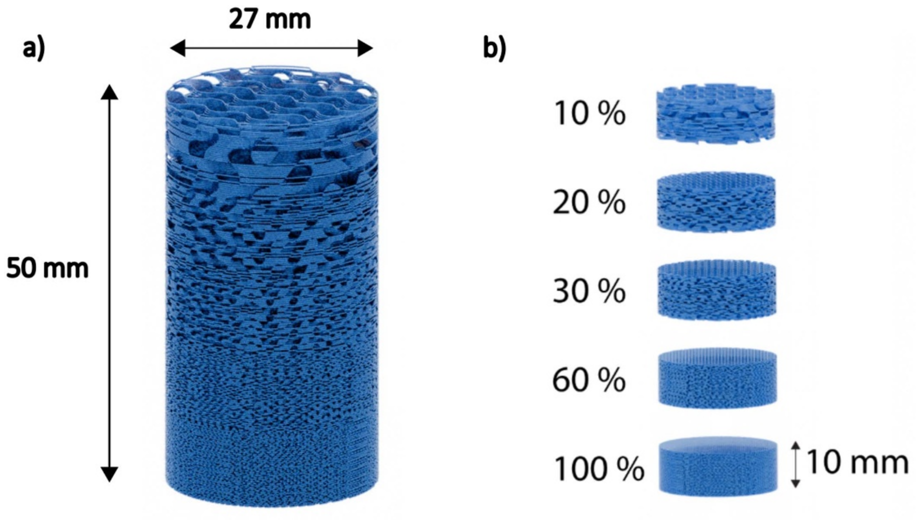

Figure 2. 3D visualisation of the cylindrical insert, (a) variable-infill density insert in full length, (b) segments of varying infill densities visualised individually.

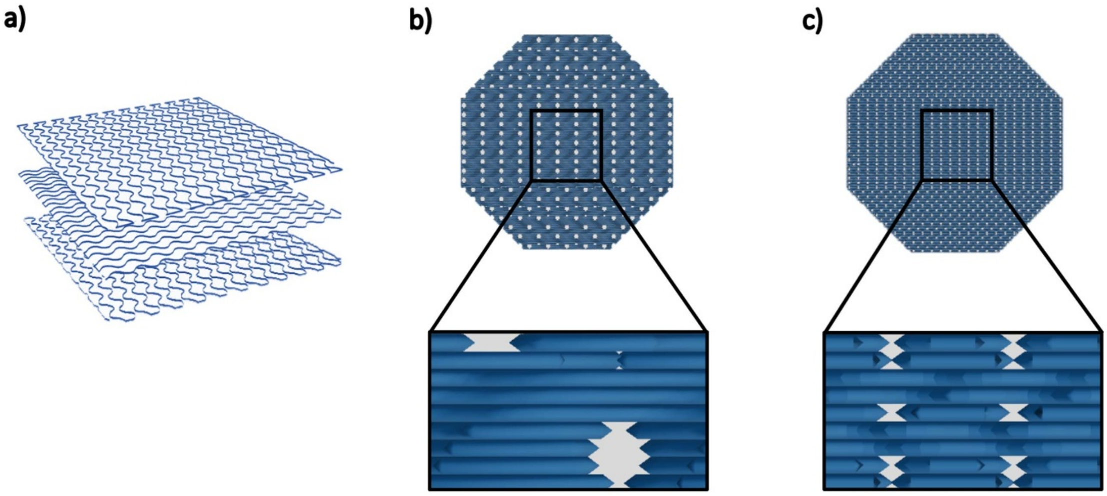

Figure 3. (a) Layers of periodic patterns that make up the gyroid lattice. The digital models of two octagonal inserts: (b) 24% infill density and (c) 50% infill density shown as top-view renderings. Air gaps extending through the full depth of the inserts appear as white regions and are clearer in the zoomed-in images.

to assess relative transmission variations, analogous to radio-chromic film measurements. This multi-modality approach enabled direct evaluation of orientation-dependent imaging and transmission properties within identical samples.

2.2.1. 3D printing of octagonal inserts

An octagonal insert with dimensions 30 mm × 30 mm × 30 mm was designed to assess infill distribution across orientations and evaluate air channel formation in the gyroid geometry. Two infill densities were used: 24% and 50%. The 24% infill was selected to mimic lung tissue. It was determined through a material calibration of multiple infill levels to match the RED of lung-mimicking materials (0.28–0.43). A 50% infill density was included to assess the impact of increased material density on air-channel visibility and anisotropy in non-solid geometries. This selection is consistent with a previous study reporting lung-mimicking CT numbers using TPU at 20%–40% infill (Hong *et al* 2020), additionally a higher infill density can be used to mimic denser, diseased regions of the lung. Both inserts were 3D-printed using Filaflex 70Navy with identical printing parameters to the variable-density cylinders (table 2). A 3D representation of the inserts is shown in figure 3.

Table 3. This table provides the protocols used in the imaging and transmission acquisitions of the 3D-printed octagonal inserts. *These dimensions were re-sampled to 0.1 mm.

Modality	Scanner/detector	Pixel size/voxel dimensions/image matrix	Acquisition parameters
Micro-CT	XRAD 225 system	Voxel size: 0.1 mm × 0.1 mm × 0.1 mm; field-of-view: 34.43 mm	Tube voltage: 50 kVp; tube current: 1.3 mA; frame rate: 5 fps; aluminium filter (2 mm)
Clinical CT	SOMATOM confidence CT scanner	Voxel size: 0.1 mm × 0.1 mm × 0.5 mm*; field-of-view: 50 mm	Tube voltage: 120 kVp; tube current: 270 mA; $\mathrm{CTDI_{vol}}$ (32 cm): 66.17 mGy; convolution kernel: Hr68h; model-based iterative reconstruction (SAFIRE)
Flat-panel detector (FPD)	PaxScan 2530HE in combination with a TrueBeam kV source	Pixel size: 0.14 mm*; image matrix: 1792 × 2176 pixels; active imaging area: 249 mm × 302 mm	**X-ray source**—tube voltage: 50 kV; tube current: 20 mA; **FPD**—frame rate: 7 fps.

2.2.2. Digital model

To obtain a digital reference, the octagonal inserts were designed and sliced using the same software as the cylindrical inserts. Slicing converts the stereolithography (STL) file, which represents only the external geometry, into a G-code file containing line-by-line printer instructions, including the internal infill pattern and filament deposition paths. The G-code was converted into a 3D mesh (OBJ) using Prusa G-code Viewer (Prusa Research, Czech Republic). This mesh which captures the actual internal structure defined by the print path, was imported into Blender v4.2.0 (Blender Foundation, The Netherlands). Blender's x-ray mode was used to inspect the internal geometry. This allowed measurement of small features, such as air channel dimensions, that may not be visible in the physical print or resolvable by available imaging systems.

Following visual inspection, the OBJ mesh was voxelised in Python using the trimesh library (Dawson-Haggerty *et al* 2022) onto a 0.1 mm grid. Voxels were assigned a value of 1 if they intersect the material region (mesh) and 0 otherwise (air), producing a strictly binary representation. This approach excludes imaging and printing artefacts, providing an idealised ground-truth geometry.

The voxelised model was generated at 0.1 mm resolution, where a single extrusion line spans approximately 2 voxels in width and 1.8 voxels in height, resulting in an array of (299, 299, 302) voxels. To verify resolution adequacy for air channel detection, the high infill model was additionally voxelised at 0.05 mm resolution for comparison.

2.2.3. CT and micro-CT imaging

Imaging was performed to evaluate anisotropy and air channels present in the octagonal inserts after 3D printing, the imaging setups for each modality and the relative scanning orientations are shown in figure 4, and the corresponding acquisition protocols are summarised in table 3. Since the digital model represents an ideal geometry, the 3D-printed inserts may differ due to the manufacturing process. Octagonal inserts were placed in custom holders, 3D-printed using a PLA filament in 100% infill density (figure 4). The 3D volumes of the inserts were reconstructed using imaging with a micro-CT and a clinical CT.

The cone-beam micro-CT (XRAD 225 System, precision x-ray Inc., USA) was included for its high resolution, whereas the clinical CT (SOMATOM Confidence) was used due to its wide availability in clinical environments, making it a feasible imaging tool for QA of 3D-printed components.

2.2.4. FPD

The FPD (PaxScan 2530HE, Varian Medical Systems, USA) was used in combination with the kilovoltage (kV) imaging source of a Varian TrueBeam system (Varian Medical Systems, USA). Positioned on the treatment couch, 1 m below the kV source. The FPD acquired 2D x-ray transmission images for each orientation by physically rotating the insert to each predefined angle. Unlike CT or micro-CT, which create volumetric reconstructions from multiple angular projections, the FPD acquires a single projection integrating attenuation effects from both transmission and scatter along the beam path. Prior to each series, a flood field image was acquired with only the holder in place to capture the detector's baseline

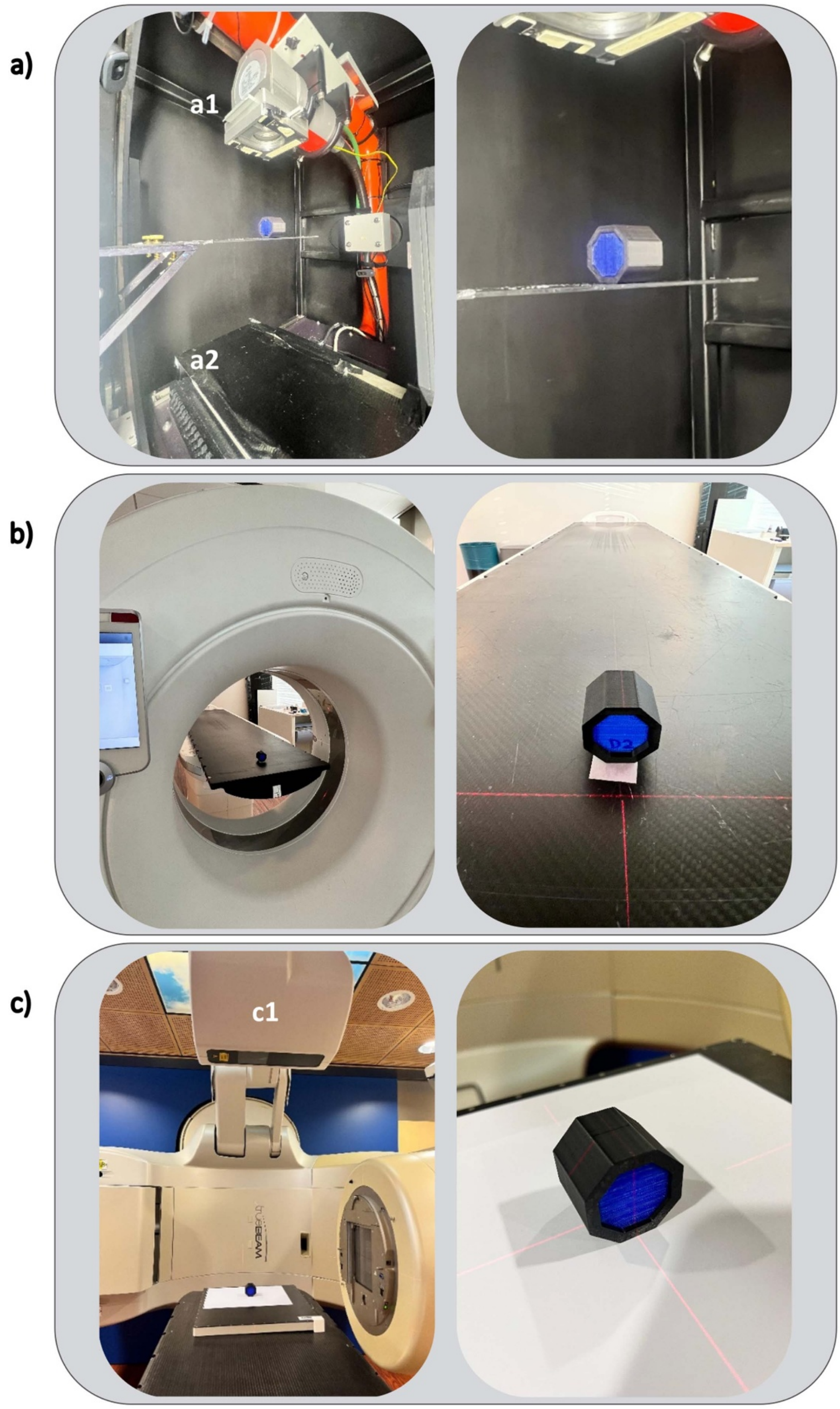

Figure 4. Imaging setup used for each modality along with the scanning orientation shown next to it. (a) Cone-beam micro-CT, the insert is placed on the stage for imaging, (a1) x-ray source and (a2) detector panel. (b) Clinical CT scanner. (c) A flat-panel detector placed on the couch with the TrueBeam system's gantry rotated 90° to use the (c1) kilovoltage x-ray source, a white paper is placed on the panel for visibility of the 3D-printed insert and positioning using lasers.

response and correct for non-uniform pixel response and electronic offsets. Images of the inserts were background-corrected by subtracting the flood field.

2.2.5. Image and data analysis

To enable cross-modality comparison and quantitative assessment of anisotropy, a standardised image analysis procedure was performed for all datasets. Volumetric reconstructions from CT and micro-CT

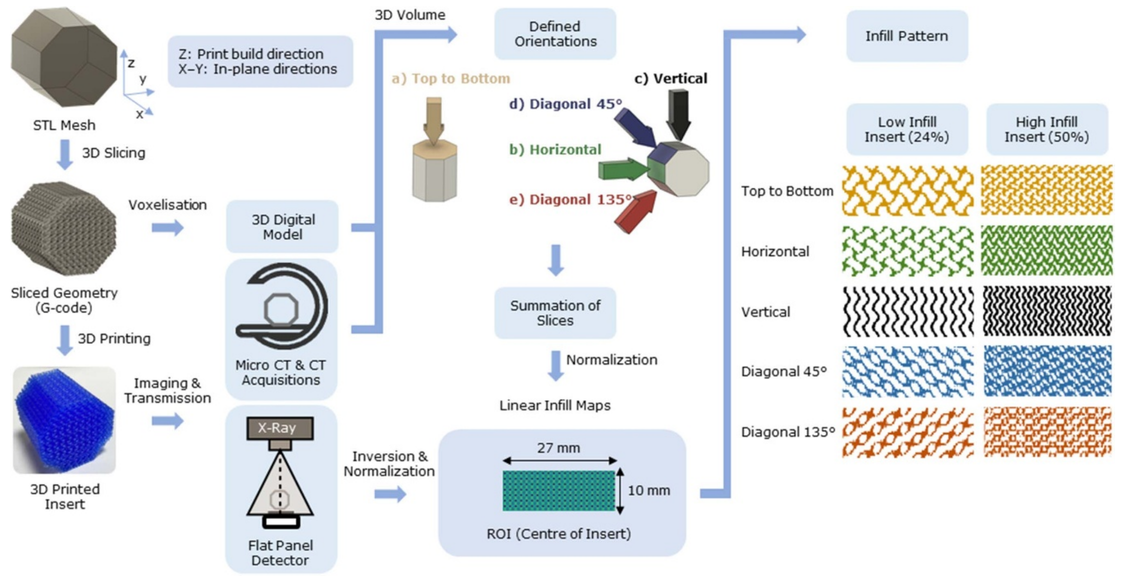

Figure 5. Workflow for generating 2D linear infill maps from the digital model and imaging modalities. The STL mesh is sliced to generate G-code and voxelised to produce a 3D digital model. The insert is then manufactured by 3D printing and imaged using micro-CT, clinical CT, and a flat-panel detector. For the digital model and reconstructed CT volumes, voxel values are integrated by digital rotation of the volume, while for the flat-panel detector the insert is physically rotated between acquisitions. Integration is performed along five orientations: (a) top-to-bottom along the printing X direction, (b) horizontal along the printing Y direction, and (c) vertical along the print build axis (Z). The diagonal orientations at 45° and 135° (d)–(e) represent oblique paths intersecting the in-plane printing directions (X and Y). The resulting 2D projections are normalised and analysed using a central region of interest (27 mm × 10 mm) to generate linear infill distribution maps. Visualisations of the infill pattern for the 24% and 50% infill inserts are shown for each orientation.

were initially resampled to a common grid with 0.1 mm isotropic voxels, in alignment with the digital model. Rigid image registration was performed to align geometries in each dataset in Python (v3.11.7), using established packages for image processing and statistical evaluation (SciPy and scikit-image) (Van Der Walt *et al* 2014, Virtanen *et al* 2020). For each insert, a central 10 mm × 27 mm ROI was defined and used in the analysis to minimise edge artefacts.

2.2.6. Linear infill distribution

Linear infill maps were generated to quantify the spatial distribution of material and air within each insert, the complete workflow is shown in figure 5. For the digital model, micro-CT and CT datasets, integration was performed by digitally rotating the volume along five orientations: horizontal, vertical, diagonal at 45°, diagonal at 135°, and top-to-bottom. These orientations are defined relative to the printing coordinates shown in the first step of figure 5. The vertical orientation follows the print build axis (Z) and corresponds to the coronal plane in imaging, while the horizontal and top-to-bottom orientations correspond to the printing Y and X directions and are acquired in the sagittal and axial planes. Diagonal orientations represent oblique paths intersecting the X–Y planes.

In the digital model, voxels were assigned binary values, 1 for material and 0 for air. Integration of these binary values through the volume depth produced maps where higher values indicated a greater proportion of material along the integration path. For the micro-CT and CT reconstructed volumes, the same digital rotation and integration procedure was applied, but using voxel values expressed in CT numbers instead of binary values. This approach simulated an idealised parallel-beam x-ray transmission through the volume.

For FPD measurements, 2D linear infill maps were acquired by physically rotating the printed insert between acquisitions, to obtain a separate projection for each orientation of the insert. FPD pixel values were inverted so that higher intensities corresponded to greater material content, consistent with the representation in CT modalities.

All linear infill maps were normalised to a 0–1 scale to enable cross-modality comparison. Air regions were assigned zero, corresponding to air voxels in the digital model, approximately −1000 HU in CT and micro-CT, and background transmission in FPD. The reference value for 100% infill material was estimated by extrapolation from inserts printed in a range of infill densities, further details are provided in the supplementary materials. The normalisation approach removes modality-specific scaling and focuses the histogram comparison on the relative infill fraction along each orientation. Because this simplifies the data into mainly air and solid regions, it is less sensitive to small details such as air channel widths. For that reason, the linear infill distribution analysis was complemented by air channel detection metrics which remain sensitive to small directional features within the volume.

Statistical evaluation was performed by constructing histograms using 20 bins spanning the 1st to 99th percentile of normalised values. Orientation-specific histogram pairs from each modality were compared using the Bhattacharyya coefficient, which quantifies distributional overlap (Bhattacharyya 1946, Pulli *et al* 2012). Pairs with coefficients exceeding 0.9 were considered highly similar. Additional metrics (differences in mean, median, standard deviation, skewness, and kurtosis) were calculated to validate the Bhattacharyya analysis. Under this normalisation, the Bhattacharyya coefficient measures how consistently each modality resolves the distribution of infill fractions across orientations.

2.2.7. Air channel detection

Air channels were evaluated from linear infill maps using the digital model as a geometric reference. It provided the expected spacing and periodicity of air channels for each infill level and orientation, where channels appear as voids defined by pixel values corresponding to air. In the imaging data, these features appear as local minima in the integrated profiles, with pixel values potentially corresponding to air or regions of reduced material density, depending on resolution.

An air channel was defined as a recurring low-density region, occurring at intervals predicted by the digital model and bounded by higher-density material. For each orientation, one-dimensional profiles were extracted from identical positions across all imaging modalities. Ten representative profiles per orientation were analysed.

Profiles were smoothed using a Gaussian filter, and valleys were detected with SciPy's find_peaks function applied to the inverted profiles. Detection criteria included a prominence threshold to isolate significant valleys and a minimum distance constraint based on the model's predicted channel spacing.

A valley was classified as an air channel if it met both the prominence and spacing criteria. Across all sampled rows, air channel width was measured, and frequency was calculated per millimetre by dividing the number of detected channels by the total profile length.

3. Results

3.1. Radiological evaluation

3.1.1. Effective atomic number

The Z_{eff} values of eleven flexible materials are presented in figure 6 along with reference lung mimicking materials from the Gammex phantom and the ICRU Report 44 (White *et al* 1989). Across all filaments, values ranged from 6.3 ± 0.6 (70Clear) to 11.1 ± 0.2 (82Skin). Differences were observed even within the same Shore hardness category. For example, two TPU 70 A materials showed contrasting results: 70Black had a Z_{eff} of 6.5 ± 0.5, whereas 70Red reached 10.5 ± 0.4.

Across all the materials, MAE in Z_{eff} relative to lung was 1.53, with values spanning from 0.14 to 3.51. The closest lung-like formulations were 78Black ($Z_{\mathrm{eff}} = 7.41, |\Delta| = 0.14$) and 63White ($Z_{\mathrm{eff}} = 7.84, |\Delta| = 0.29$)). In contrast, some materials indicated a higher Z_{eff} such as 82Skin ($Z_{\mathrm{eff}} = 11.06, |\Delta| = 3.51$) and 70Red ($Z_{\mathrm{eff}} = 10.46, |\Delta| = 2.91$) which deviate strongly from the reference.

Seven filaments (63White, 63Black, 70Black, 70Clear, 70Navy, 78Black, and 78Natural) were identified as the most lung-like and selected for further RED analysis. Within this subset, the MAE in Z_{eff} was substantially lower, at 0.78, confirming that their Z_{eff} values cluster closely around the reference.

3.1.2. RED

The RED for regions with infill density ranging from 10% to 100% was evaluated, ranging from 0.11 to 1.07, as shown in figure 7. These values include the expected range for reference lung materials, including LN300 (RED = 0.28), LN450 (RED = 0.43), and lung parenchyma (RED = 1.04). Across the seven selected filaments, RED decreased consistently with infill reduction, while 100% infill regions remained close to water equivalence. Standard deviations were generally small, indicating stable voxel-to-voxel reproducibility, although a greater spread was observed at intermediate infill densities.

3.2. Anisotropy evaluation

The anisotropy of the octagonal inserts was evaluated across five projection orientations: horizontal, vertical, diagonal 45°, diagonal 135°, and top-to-bottom. Results are presented for low (24%) and high (50%) infill densities.

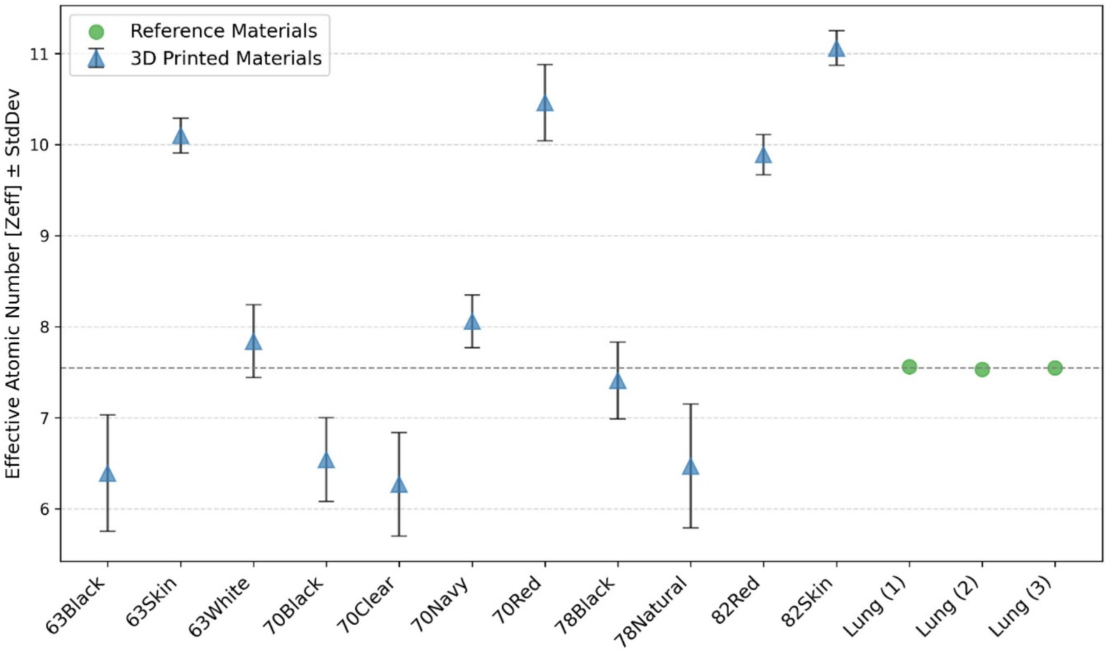

Figure 6. Effective atomic number (Z_{eff}) of the investigated 3D printing materials compared with lung mimicking references, a dashed line indicating the mean references at 7.55. The reference Z_{eff} value reported is calculated based on theoretical elemental composition, therefore no standard deviation is plotted. Lung 1 and Lung 2 are the 'LN300 Lung' and 'LN450 Lung' from the Gammex Advanced Electron Density Phantom and Lung 3 is 'Lung Parenchyma' as reported in ICRU Report 44.

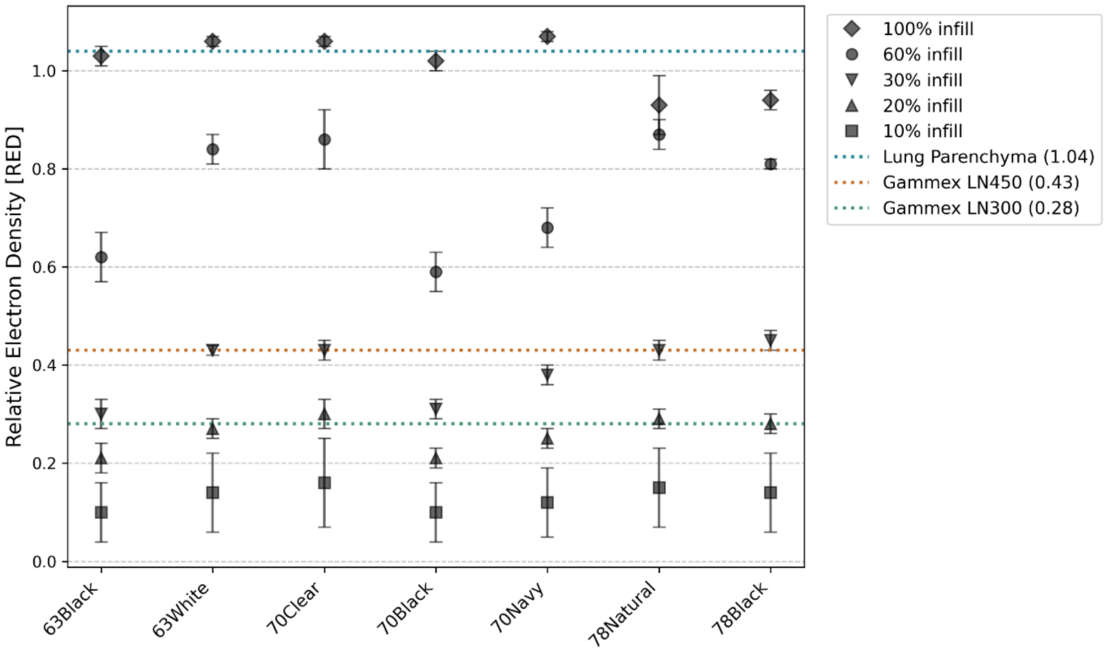

Figure 7. Relative electron density (RED) of seven flexible TPU filaments as a function of infill density. Data points represent the mean RED ± one standard deviation, where the standard deviation reflects voxel-to-voxel variation in estimated RED within the imaged region of interest. The obtained RED values for 20%–30% infill densities show agreement with reference lung-mimicking materials (LN300 and LN450).

3.2.1. Linear infill distribution

The linear infill maps for the horizontal orientation and corresponding histograms for both low- and high-infill inserts are shown in figure 8. These were generated using the digital model, micro-CT, CT, and FPD. Visual comparison shows that for the low-infill insert (figure 8(a)) the digital model shows a well-defined periodic material distribution pattern, which is also resolved by all three imaging systems.

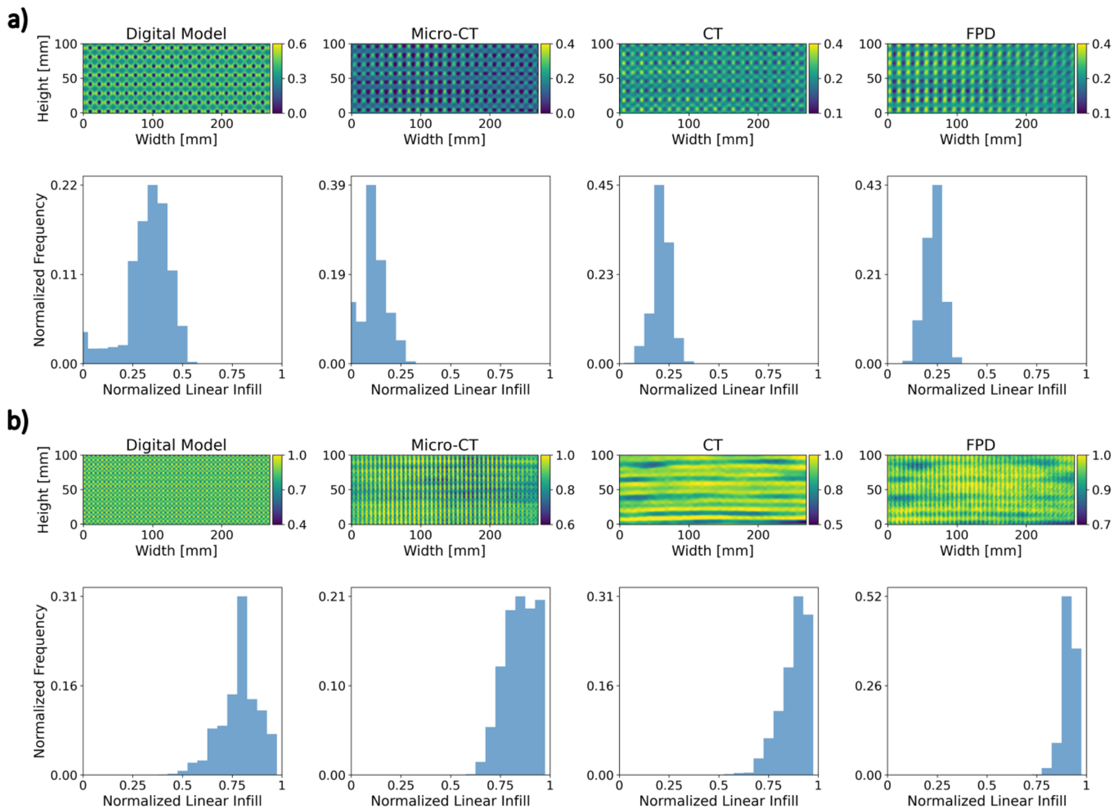

Figure 8. Linear infill maps and corresponding histograms for the horizontal orientation are shown for (a) low and (b) high infill inserts, obtained from the digital model, micro-CT, CT, and FPD. Infill maps are normalised from 0 (air) to 1 (100% infill). Brighter regions indicate higher material content, and darker regions indicate lower infill or air gaps. This visualisation enables the comparison of structural resolution, infill distribution, and modality-dependent differences.

For the high-infill insert (figure 8(b)), the digital model again displays the expected periodic pattern, while micro-CT and FPD partially resolve this pattern, and CT does not resolve it.

Horizontal streaks are visible in the infill maps of all three imaging systems for both inserts. The histograms below each map show the distribution of normalised linear infill values per modality. Histogram peak shifts reflect the proportion of air and material in the infill map, with imaging systems indicate different distributions from the digital model. Infill maps for additional orientations are provided in the supplementary materials.

Figure 9 shows heatmaps of Bhattacharyya coefficients for pairwise comparisons of linear infill histograms between orientations for each modality.

For the low-infill insert (figure 9(a)), the digital model shows near-isotropic behaviour with coefficients above 0.91 for most orientation pairs, and moderate anisotropy with coefficients (0.76–0.79) between diagonal and non-diagonal orientations. CT results show clear anisotropy, with six out of ten pairs below 0.90. All modalities show high isotropy between diagonal pairs.

For the high-infill insert (figure 9(b)), the digital model is mostly isotropic, with minor anisotropy in the top-to-bottom–diagonal45° pair (0.89). Micro-CT and FPD maintain high isotropy with all coefficients above 0.94. In contrast, CT shows pronounced anisotropy, with low coefficients (0.56–0.67) for horizontal–vertical and horizontal-diagonal comparisons, likely due to resolution limitations.

3.2.2. Air channel detection

Line profiles extracted from the linear infill maps are shown in figure 10. Each plot displays two representative profiles, one from each insert. The profiles illustrate the integrated material and air content along the depth of the octagonal inserts. Based on the known air channel spacing from the digital model, valleys representing regions of low material density that appear at the same periodic positions and lie between two material-rich peaks were identified as air channels, even when the valleys of the line profile did not reach zero.

At low infill, all modalities show clear periodic oscillations. In the digital model, valleys reach zero (air) only in orthogonal orientations. The imaging systems reproduce the periodic pattern with a reduced amplitude, with FPD and CT valleys not reaching zero except in the top-to-bottom orientation.

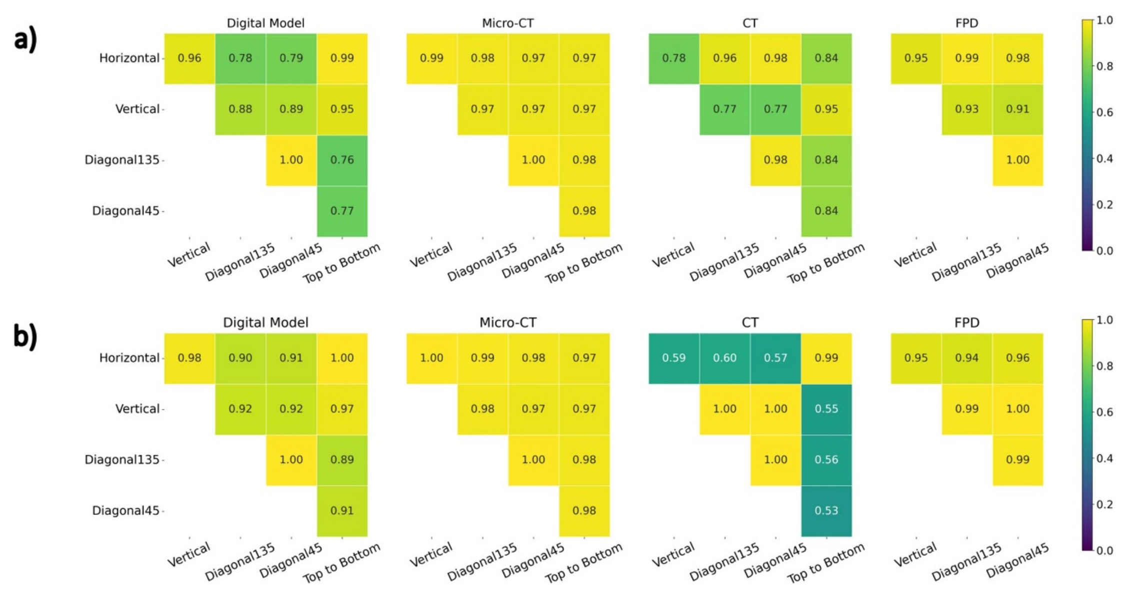

Figure 9. Pairwise Bhattacharyya coefficients for linear infill histograms similarity between five orientations. (a) Low infill and (b) high infill inserts. Higher coefficients (yellow) indicate greater similarity between orientation pairs, while lower values (green/blue) indicate lower similarity. The modalities are shown individually to assess directional uniformity within each modality.

At high infill, all modalities exhibit higher baseline values, and the imaging systems show a lower peak-to-valley ratio compared to the low-infill insert. Micro-CT and FPD still resolve the periodic pattern and detect regions of low material content at the expected positions, whereas CT profiles show shallow oscillations that fail to resolve all air channels represented in the digital model.

The air channel widths and frequency for each modality and orientation are visualised in figure 11. At low infill (figure 11(a)), the digital model reports channel widths of approximately 0.7 mm. Micro-CT, CT and FPD detect channels at matching periodic positions and report comparable widths, with the exception of micro-CT which overestimated some channels widths. At high infill (figure 11(b)), the digital model indicates narrower channels of about 0.3 mm. Micro-CT and FPD detect air channels width and spacing that are comparable to the digital model, while CT overestimates channel width and shows increased orientation-dependent variability.

To verify resolution effects, the high infill digital model was regenerated at 0.05 mm voxel size. In this case, valleys reached zero in horizontal and top-to-bottom orientations, while the vertical orientation remained above zero. Manual measurements from the 3D mesh confirmed a vertical channel width of 0.05 mm. These findings show that all three imaging systems were able to resolve air-channel periodicity in the low-infill insert, with micro-CT showing the sharpest and most clearly defined profiles. At higher infill densities, micro-CT and FPD still resolved the periodic pattern, whereas CT showed reduced sensitivity, with several channels not detected. While micro-CT measured slightly larger air-channel widths in some orientations.

4. Discussion

This study evaluated flexible TPU materials for their suitability in 3D-printed dynamic lung phantoms by assessing their radiological properties, anisotropy, and internal air-channels across imaging modalities. Seven of the eleven materials fell within lung-mimicking Z_{eff} and RED ranges. Linear infill maps showed that low-infill gyroid structures contained distinct air channels that all modalities could detect, while the much narrower channels in high-infill samples were not visible in the clinical CT. The digital model provided a reference for identifying internal structure and orientation-dependence before printing and imaging.

This study supports the development of 3D-printed lung phantoms, where candidate materials are typically evaluated using CT numbers or RED to achieve lung-mimicking properties (Hazelaar *et al* 2018, Bustillo *et al* 2019, Hernandez-Giron *et al* 2019, Shin *et al* 2020, Hatamikia *et al* 2022, Tino *et al* 2022, Kunert *et al* 2023, Abdollahi *et al* 2024, Bakhtiari Moghaddam *et al* 2025), by providing a comprehensive radiological evaluation that emphasises the importance of assessing material composition. This study also

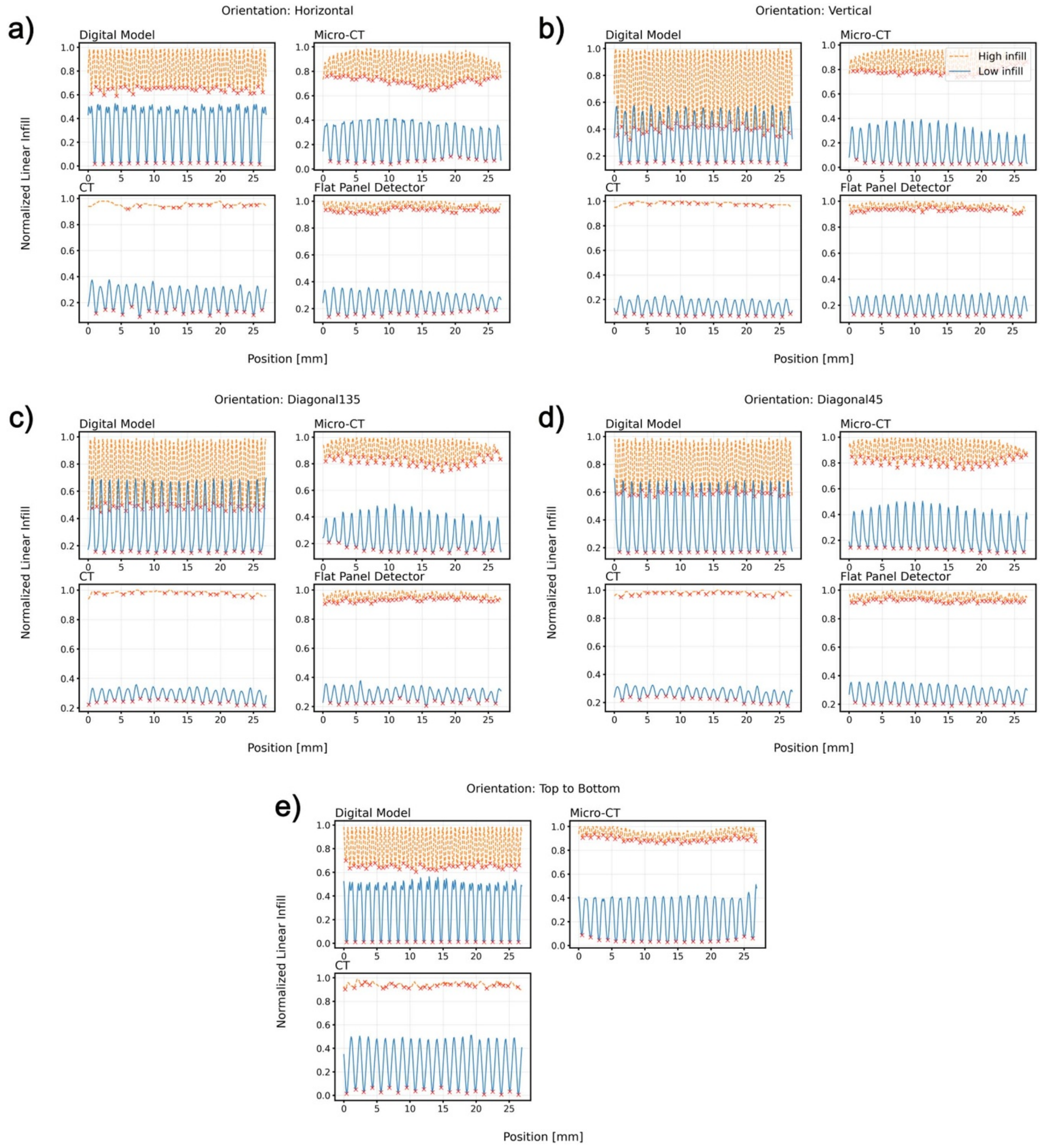

Figure 10. Line profiles extracted from normalised linear infill maps of the digital model, micro-CT, CT, and flat-panel detector for five orientations: (a) horizontal, (b) vertical, (c) diagonal 135°, (d) diagonal 45°, and (e) top-to-bottom. A line profile is sampled from both low- (blue) and high- (orange) infill inserts from a single row within the region of interest. Red crosses mark the detected air channels.

presents an advanced evaluation of anisotropy and quantification of air channels in 3D-printed geometries, which were identified by earlier work (Madamesila *et al* 2016, Tino *et al* 2019, Fonseca *et al* 2023), and further evaluated in this study through multiple imaging modalities, offering a better understanding of the internal structure of 3D-printed phantoms.

4.1. Radiological and physical properties evaluation

The presence of air gaps lowers the RED and may therefore affect the CT-to-density calibration. However, these gaps have limited impact on the average Z_{eff}, since air ($Z_{\mathrm{eff}} = 7.66$) is comparable to that of carbon-based polymers (Z_{eff} around 6–7) (Singh and Badiger 2014). Several materials have Z_{eff} values comparable to reference lung materials ($Z_{\mathrm{eff}} = 7.55$), although some materials have a much higher Z_{eff} and are not suitable for dosimetric applications in radiotherapy, but may still be useful for imaging phantoms where accurate electron density is less critical (Lustermans *et al* 2024). Additionally, materials of the same category but in a different colour exhibited varying Z_{eff} values, indicate that differences in atomic composition could possibly be due to pigment, as also observed in previous studies (Ma *et al* 2021, Fonseca *et al* 2023).

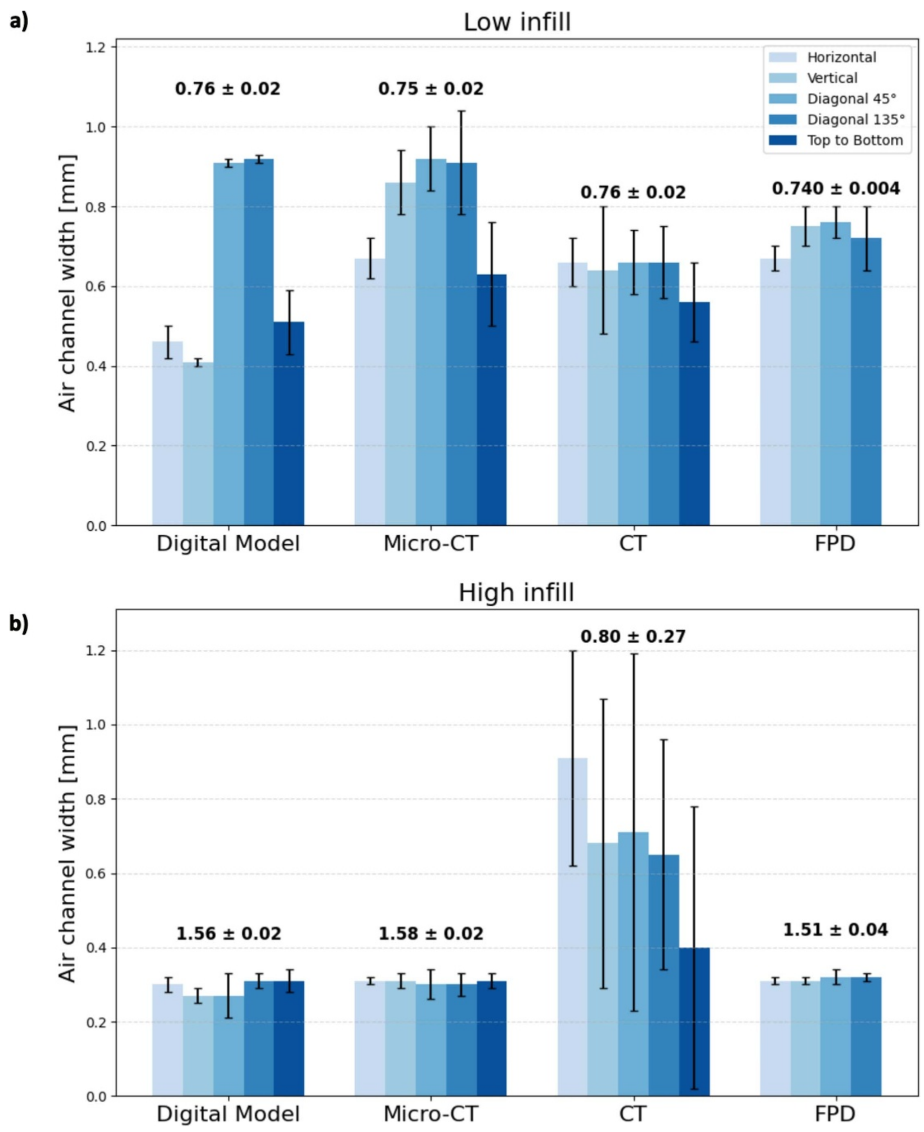

Figure 11. Air channel widths and frequencies for the low (a) and high infill (b) octagonal inserts. The mean channel width (bar height) and standard deviation (error bars) are shown across five orientations for each imaging system. The mean air-channel frequency (channels per mm) is labelled above each group. There was no acquisition done using the flat-panel detector for the top-to-bottom orientation.

Results showed that target RED values for reference lung materials can be achieved using infill densities of approximately 20%–40%, depending on the material selected. Denser structures, such as lung lesions, can be modelled using 100% infill for most materials, except for 78Natural and 78Black, which exhibited RED values below 1.0 even at full infill. At 60% infill, the measured RED varied considerably between materials, likely due to differences in material formulation. The observed variation may also arise from print-related inconsistencies, where deviations in extrusion rate alter the effective material fraction within the scanned volume, leading to shifts in the estimated RED. To minimise this effect, all inserts in this study were manufactured using a single 3D printer. The observed variation in RED for identical infill levels and print settings indicate that a specific infill percentage cannot universally represent lung tissue, and that material-specific calibration is required prior to phantom use.

To verify reproducibility, several inserts were reprinted for selected materials. Across these, RED values were reproduced within ±0.05 of the original measurement, confirming that the differences between independent prints remained within expected experimental uncertainty. Given this high consistency, not all materials were reprinted for validation.

To manufacture lung-mimicking phantoms, the recommended approach is to first select a filament with a measured Z_{eff} close to the lung reference value, such as 78Black, 70Navy, 63White. Then, select a low infill density within the calibration range in figure 7, manufacture test prints and adjust the infill, if necessary, until desired RED is achieved. Test prints are best evaluated using the highest resolution imaging modality available. Optimal uniformity and repeatable RED values are most reliably achieved by using consistent printer settings optimised for the specific filament in use, and by printing on the same machine, then validating the final print through imaging.

Achieving a uniform material distribution at low infill density is challenging with TPU. Stringing, nozzle clogs, and filament build-up can lead to over- or under-extrusion, creating clusters of high or low density that break print uniformity. To limit these artefacts, layer height, flow rate, print speed, and extrusion width must be set with care, and the ideal settings identified through an optimisation process for each filament individually. A layer height close to 60% of the nozzle diameter, combined with a slightly wider extrusion width and reduced print speed, has been shown to improve line fusion and reduce unintended air gaps (Jang *et al* 2021, Tao *et al* 2021, Mohseni *et al* 2023).

Overall, this workflow demonstrates that with careful selection of filament material and tuning of print parameters, it is possible to closely approximate the RED and Z_{eff} of human lung and reference materials in 3D-printed phantoms. For precise CT-to-density calibration and dosimetric accuracy, 3D printing settings must be standardised, printers carefully calibrated, and verification imaging routinely performed to assess object uniformity and internal structure prior to use in radiotherapy QA.

4.2. Anisotropy evaluation

The digital model driven workflow for evaluation of 3D-printed phantoms used in this study, can streamline the iterative cycle of designing, printing, scanning, quantitative evaluation, and tuning of printing settings (Mei *et al* 2022, Okkalidis *et al* 2022). Voxelised meshes may be evaluated as projections, they may also be incorporated into Monte Carlo simulations to calculate dosimetric effects of specific print parameters such as different infill patterns (Campbell *et al* 2025). Dimensional differences between the design file and the sliced geometry can occur when the selected layer height and extrusion width do not evenly divide across the model, as the software constrains dimensions to multiples of extrusion width and layer height. The sliced model was 0.06 mm taller and 0.19 mm narrower than the STL design. The discrepancies were below 2% and were acceptable given the 0.1 mm voxel resolution. A finer voxelisation (0.05 mm) can improve representation of sub-millimetre channels but would increase computational cost.

4.2.1. Linear infill distribution

The gyroid infill geometry is mathematically near-isotropic, however, anisotropies may appear due to factors such as the 3D-printing process, sampling resolution, and the imaging system used (Li *et al* 2023, Sarmiento-O’Meara *et al* 2025). In the digital model, small directional differences appear mainly at diagonal orientations (45° and 135°), while orthogonal orientations do not indicate a high difference. The variation in the diagonals may be due to discretisation effects where the diagonal path integrating voxels along the depth intersects a different proportion of air and material voxels than the orthogonal orientations. This results in a variation in the histograms spread, which is numerical and not present in the physical geometry. All the modalities indicated a similarity between the top-to-bottom and the horizontal orientations, which can be attributed to both intersecting the layer stacking perpendicularly and therefore producing a comparable air-material distribution.

The micro-CT and FPD indicated highly similar distributions across orientations in the printed inserts, with micro-CT showing a more visible variation in histograms distribution than the FPD. Micro-CT reconstructs attenuation from hundreds of projections, where each voxel value is derived from all viewing angles. The Bhattacharyya coefficients demonstrate that the printed insert does not exhibit orientation dependence in high resolution imaging, specifically isotropic resolution in the case of the micro-CT.

In contrast, the CT indicated apparent anisotropy, likely influenced by its inherently anisotropic spatial resolution, where axial averaging limited by slice thickness leads to orientation-dependent partial-volume effects (International Commission on Radiological Protection 2007, Samei *et al* 2019). This mainly affects the vertical orientation through reduced contrast and CT number range, while diagonal orientations are influenced by combined axial and in-plane sampling. Changing the imaging orientation resulted in histogram range variations of up to 60% (supplementary materials), confirming that the observed anisotropy arises from orientation-dependent sampling and partial-volume averaging rather than the 3D-printed geometry.

A limitation of this work is that the evaluation was performed under static conditions only. Under breathing-like motion, CT attenuation and the apparent size of air channels may change. Deformable 3D-printed lung phantoms show that compression can shift measured CT attenuation and alter the apparent size of air-filled structures, so the static results here should be interpreted as a best-case assessment of air-channel visibility (Shin *et al* 2020, Im *et al* 2025). Similarly, CT studies of human lungs report measurable changes in airway dimension between inhalation and exhalation (Hu *et al* 2023, Jing *et al* 2025). Resolving air channels under these conditions would require high spatial and temporal resolution, since the air channel sizes observed in this study are close to the detection limits of clinical imaging systems.

4.2.2. Air channel detection

Visual inspection of the 3D geometry prior to 3D printing revealed that both low and high infill inserts contained continuous air channels. For the low-infill insert, the measured width of the air channels was 0.7 mm, which was well above the spatial resolution of all the modalities. For the high-infill insert, the air channels had a width of approximately 0.3 mm. At this scale, detection is challenging because of the limited number of voxels spanning the channel width; therefore, even with high spatial resolution imaging, no pure air voxels were detected for these air channels.

The results show agreement between all modalities on the frequency of air channels per mm at both infill levels, except for CT, which missed many air channels in the high infill insert owing to its inherent detection limits. The CT has a 2 cm detector with 0.6 mm collimation; therefore, air channels with a width of 0.3 mm would fall below the system's detectable spatial resolution (Siemens Healthineers 2019).

At low infill, the air channel width measured using the imaging systems was slightly higher than that in the digital model for the orthogonal orientations. This can be explained by the sharp binary edges of the digital model, whereas imaging systems produce blurred transitions due to their point-spread function. At a high infill, the air channels were narrower and approached the imaging-resolution limit. The valleys indicating air regions (figure 10) span fewer voxels and exhibit a lower dynamic range due to signal contributions from neighbouring material voxels. Consequently, the width was estimated from the extent of the low-density region rather than the pure air voxels. Both micro-CT and FPD show strong agreement with the digital model, confirming that they resolve the channels accurately within this scale. In contrast, CT shows substantial variability and overestimation of channel width owing to its limited axial-plane resolution and partial-volume averaging, which may combine neighbouring low-density zones into broader apparent air channels.

These results highlight the importance of high-resolution imaging for the accurate characterisation of 3D-printed samples. Micro-CT and FPD demonstrated the most reliable performance, consistently resolving air channels and reproducing digital model dimensions with low variations. This is consistent with previous work reporting that gyroid-based 3D-printed structures scanned using a clinical CT with 0.4 mm in-plane resolution and 1 mm slice thickness exhibited homogenous CT profiles, where air channels were unresolved (Fonseca *et al* 2023). Coarse-resolution acquisitions are acceptable when the features of interest are larger than the voxel size; however, when feature sizes approach the imaging resolution, partial-volume averaging may obscure a possible structural heterogeneity (Leary *et al* 2020). Although potential dosimetric effects were not assessed in this study, they should be quantified in future work for radiotherapy phantom validation and QA applications.

5. Conclusion

This study demonstrated that TPU filaments can reproduce lung-mimicking radiological properties that are suitable for 3D-printed dynamic phantoms. The digital model driven workflow can be useful for dosimetric evaluation in Monte Carlo simulations. Anisotropy was indicated by the digital model only in non-orthogonal orientations. In contrast, micro-CT and FPD indicated near-isotropy, whereas CT exhibited apparent anisotropy due to modality-specific limitations. Among the imaging systems, micro-CT and FPD accurately resolved the air channels, with some variation due to blurring. CT overestimated the width of air channels that were narrower than its detection ability. Overall, micro-CT is the most reliable modality for evaluating anisotropy and small internal features, FPD can be used as a practical substitute, and CT provides useful but limited information for clinical-scale assessments. The workflows and findings of this study support the process of verifying internal geometry, optimising print parameters, and reducing trial-and-error in phantom manufacturing to ensure consistent performance and prevent potential dosimetric deviations in radiotherapy QA.

Data availability statement

The data cannot be made publicly available upon publication because they are not available in a format that is sufficiently accessible or reusable by other researchers. The data that support the findings of this study are available upon reasonable request from the authors.

Supplementary-materials available at https://doi.org/10.1088/1361-6560/ae456d/data1.

ORCID iDs

Roua Abdulrahim 0009-0001-3990-7967
Didier Lustermans 0000-0002-3067-5645
Murillo Bellezzo 0000-0001-5273-0003
Behzad Rezaeifar 0000-0002-2125-1154
Brigitte Reniers 0000-0001-7084-4696
Frank Verhaegen 0000-0001-8470-386X
Gabriel Paiva Fonseca 0000-0002-8087-1193

References

Abdollahi S, Mowlavi A A, Yazdi M H H, Ceberg S, Aznar M C, Tabrizi F V, Salek R, Guckenberger M and Tanadini-Lang S 2024 Dynamic anthropomorphic thorax phantom for quality assurance of motion management in radiotherapy *Phys. Imaging Radiat. Oncol.* **30** 100587

Bakhtiari Moghaddam A *et al* 2025 A dynamic anthropomorphic phantom for end-to-end testing in image- and surface-guided adaptive radiotherapy *Med. Phys.* **52** e70107

Bhattacharyya A 1946 On a measure of divergence between two multinomial populations *Sankhya* **7** 401–6

Bustillo J P O, Mata J L, Posadas J R D, Inocencio E T, Rosenfeld A B and Lerch M L F 2025 Characterization and evaluation methods of fused deposition modeling and stereolithography additive manufacturing for clinical linear accelerator photon and electron radiotherapy applications *Phys. Med.* **130** 104904

Bustillo J P, Tumlos R and Remoto R Z 2019 Intensity modulated radiotherapy (IMRT) phantom fabrication using fused deposition modeling (FDM) 3D printing technique *World Congress on Medical Physics and Biomedical Engineering 2018* ed L Lhotska, L Sukupova, I Lacković and G S Ibbott (Springer) pp 509–15

Campbell M C, Pollmann S I, Milner J S, Lalone E A and Holdsworth D W 2025 A novel method to simulate radiographs of 3D printed objects *J. Appl. Clin. Med. Phys.* **26** e70159

Chacón J M, Caminero M A, García-Plaza E and Núñez P J 2017 Additive manufacturing of PLA structures using fused deposition modelling: effect of process parameters on mechanical properties and their optimal selection *Mater. Des.* **124** 143–57

Craft D F and Howell R M 2017 Preparation and fabrication of a full-scale, sagittal-sliced, 3D-printed, patient-specific radiotherapy phantom *J. Appl. Clin. Med. Phys.* **18** 285–92

Dancewicz O L, Sylvander S R, Markwell T S, Crowe S B and Trapp J V 2017 Radiological properties of 3D printed materials in kilovoltage and megavoltage photon beams *Phys. Med.* **38** 111–8

Dawson-Haggerty M *et al* 2022 Trimesh: a Python library for triangular meshes (available at: https://trimesh.org/)

Dunn L, Kron T, Johnston P N, McDermott L N, Taylor M L, Callahan J and Franich R D 2012 A programmable motion phantom for quality assurance of motion management in radiotherapy *Australas. Phys. Eng. Sci. Med.* **35** 93–100

Fonseca G P, Rezaeifar B, Lackner N, Haanen B, Reniers B and Verhaegen F 2023 Dual-energy CT evaluation of 3D printed materials for radiotherapy applications *Phys. Med. Biol.* **68** 035005

Garg N, Rastogi V and Kumar P 2022 Process parameter optimization on the dimensional accuracy of additive manufacture thermoplastic polyurethane (TPU) using RSM *Mater. Today* **62** 94–99

Gebisa A and Lemu H 2018 Investigating effects of fused-deposition modeling (FDM) processing parameters on flexural properties of ULTEM 9085 using designed experiment *Materials* **11** 500

Hatamikia S *et al* 2022 3D printed patient-specific thorax phantom with realistic heterogenous bone radiopacity using filament printer technology *Z. Med. Phys.* **32** 438–52

Hazelaar C, Van Eijnatten M, Dahele M, Wolff J, Forouzanfar T, Slotman B and Verbakel W F A R 2018 Using 3D printing techniques to create an anthropomorphic thorax phantom for medical imaging purposes *Med. Phys.* **45** 92–100

Hernandez-Giron I, Den Harder J M, Streekstra G J, Geleijns J and Veldkamp W J H 2019 Development of a 3D printed anthropomorphic lung phantom for image quality assessment in CT *Phys. Med.* **57** 47–57

Hohimer C, Christ J, Aliheidari N, Mo C and Ameli A 2017 3D printed thermoplastic polyurethane with isotropic material properties *SPIE Smart Structures and Materials + Nondestructive Evaluation and Health Monitoring* ed N C Goulbourne (*Portland, Oregon, United States*) p 1016511 (available at: http://proceedings.spiedigitallibrary.org/proceeding.aspx?doi=10.1117/12.2259810)

Holmes D W, Singh D, Lamont R, Daley R, Forrestal D P, Slattery P, Pickering E, Paxton N C, Powell S K and Woodruff M A 2022 Mechanical behaviour of flexible 3D printed gyroid structures as a tuneable replacement for soft padding foam *Addit. Manuf.* **50** 102555

Hong D, Lee S, Kim G B, Lee S M, Kim N and Seo J B 2020 Development of a CT imaging phantom of anthromorphic lung using fused deposition modeling 3D printing *Medicine* **99** e18617

Hu W-T, Chen W, Zhou M, Fan J, Yan F, Liu B, Lu F-Y, Chen R, Guo Y and Yang W 2023 Quantitative analyzes of the variability in airways via four-dimensional dynamic ventilation CT in patients with chronic obstructive pulmonary disease: correlation with spirometry data and severity of airflow limitation *J. Thorac. Dis.* **15** 4775–86

Hünemohr N, Krauss B, Tremmel C, Ackermann B, Jäkel O and Greilich S 2014 Experimental verification of ion stopping power prediction from dual energy CT data in tissue surrogates *Phys. Med. Biol.* **59** 83–96

Hurkmans C W, Van Lieshout M, Schuring D, Van Heumen M J T, Cuijpers J P, Lagerwaard F J, Widder J, Van Der Heide U A and Senan S 2011 Quality assurance of 4D-CT scan techniques in multicenter phase III trial of surgery versus stereotactic radiotherapy (radiosurgery or surgery for operable early stage (stage 1A) non-small-cell lung cancer [ROSEL] study) *Int. J. Radiat. Oncol.* **80** 918–27

Im J Y, Micah N, Perkins A E, Mei K, Geagan M, Roshkovan L and Noël P B 2025 PixelPrint4D: a 3D printing method of fabricating patient-specific deformable CT phantoms for respiratory motion applications *Invest. Radiol.* **60** 636–46

International Commission on Radiological Protection 2007 Managing patient dose in multi-detector computed tomography (MDCT) *Ann. ICRP* **37**(**1**) 1–79

Jang S, Boddorff A, Jang D J, Lloyd J, Wagner K, Thadhani N and Brettmann B 2021 Effect of material extrusion process parameters on filament geometry and inter-filament voids in as-fabricated high solids loaded polymer composites *Addit. Manuf.* **47** 102313

Jing S, Liu C, Zhang J, Mu J, He L and Hou R 2025 Quantitative CT measurements of segmental bronchial changes during inspiratory and expiratory phases in healthy subjects *BMC Pulm. Med.* **25** 353

Kunert P, Schlattl H, Trinkl S, Giussani A, Klein L, Janich M, Reichert D and Brix G 2023 Reproduction of a conventional anthropomorphic female chest phantom by 3D-printing: comparison of image contrasts and absorbed doses in CT *Med. Phys.* **50** 4734–43

Leary M, Tino R, Keller C, Franich R, Yeo A, Lonski P, Kyriakou E, Kron T and Brandt M 2020 Additive manufacture of lung equivalent anthropomorphic phantoms: a method to control Hounsfield number utilizing partial volume effect *J. Eng. Sci. Med. Diagn. Ther.* **3** 011001

Lee H, Eom R and Lee Y 2019 Evaluation of the mechanical properties of porous thermoplastic polyurethane obtained by 3D printing for protective gear *Adv. Mater. Sci. Eng.* **2019** 5838361

León-Calero M, Reyburn Valés S C, Marcos-Fernández Á and Rodríguez-Hernandez J 2021 3D printing of thermoplastic elastomers: role of the chemical composition and printing parameters in the production of parts with controlled energy absorption and damping capacity *Polymers* **13** 3551

Li N, Xue C, Chen S, Aiyiti W, Khan S B, Liang J, Zhou J and Lu B 2023 3D printing of flexible mechanical metamaterials: synergistic design of process and geometric parameters *Polymers* **15** 4523

Lustermans D, Abdulrahim R, Taasti V T, Szkitsak J, Švėgždaitė E, Clarkin S, Reniers B, Verhaegen F and Paiva Fonseca G 2024 Development of a novel 3D-printed dynamic anthropomorphic thorax phantom for evaluation of four-dimensional computed tomography *Phys. Imaging Radiat. Oncol.* **32** 100656

Lustermans D, Fonseca G P, Jeukens C, Taasti V T, Parodi K, Landry G and Verhaegen F 2025 Evaluating photon-counting computed tomography for quantitative material characteristics and material differentiation in radiotherapy *Phys. Med. Biol.* **70** 105013

Ma X, Buschmann M, Unger E and Homolka P 2021 Classification of x-ray attenuation properties of additive manufacturing and 3D printing materials using computed tomography from 70 to 140 kVp *Front. Bioeng. Biotechnol.* **9** 763960

Madamesila J, McGeachy P, Villarreal Barajas J E and Khan R 2016 Characterizing 3D printing in the fabrication of variable density phantoms for quality assurance of radiotherapy *Phys. Med.* **32** 242–7

Martín-Sosa E, Távara L, Ojeda J and Estefani A 2025 Anisotropic and hyperelastic mechanical response of 3D printed TPU parts *Prog. Addit. Manuf.* **10** 5697–709

McGarry C K *et al* 2020 Tissue mimicking materials for imaging and therapy phantoms: a review *Phys. Med. Biol.* **65** 23TR01

Mei K, Geagan M, Roshkovan L, Litt H I, Gang G J, Shapira N, Stayman J W and Noël P B 2022 Three-dimensional printing of patient-specific lung phantoms for CT imaging: emulating lung tissue with accurate attenuation profiles and textures *Med. Phys.* **49** 825–35

Mohseni Y, Mohseni M, Suresh S, Riotto M, Jaggessar A, Little J P, Wille M-L and Yarlagadda P K 2023 Investigating impacts of FDM printing parameters and geometrical features on void formation in 3D printed automotive components *Mater. Today* (https://doi.org/10.1016/j.matpr.2023.06.078)

Okkalidis N, Bliznakova K and Kolev N 2022 A filament 3D printing approach for CT-compatible bone tissues replication *Phys. Med.* **102** 96–102

Öllers M C, Swinnen A C C and Verhaegen F 2020 Acuros® dose verification of ultrasmall lung lesions with EBT-XD film in a homogeneous and heterogeneous anthropomorphic phantom setup *Med. Phys.* **47** 5829–37

Pulli K, Baksheev A, Kornyakov K and Eruhimov V 2012 Real-time computer vision with OpenCV *Commun. ACM* **55** 61–69

Saito M, Kawakami H, Suzuki T, Suzuki H, Ueda K, Nemoto H, Sano N and Onishi H 2023 Development of a dynamic motion platform with two independent drive systems for radiotherapy *J. Appl. Clin. Med. Phys.* **24** e13971

Samei E *et al* 2019 *Performance Evaluation of Computed Tomography Systems* (American Association of Physicists in Medicine) (available at: www.aapm.org/pubs/reports/RPT_233.pdf)

Sarmiento-O'Meara J, Torrente-Prato G, Olaya-Florez J and León-Molina H 2025 Orthotropic compressive behavior of the gyroid lattice structure of PLA produced via material extrusion additive manufacturing *Next Mater.* **9** 101156

Schiefer H *et al* 2010 The Swiss IMRT dosimetry intercomparison using a thorax phantom *Med. Phys.* **37** 4424–31

Sevillano D, Núñez L M, Chevalier M and García-Vicente F 2020 Definition of internal target volumes based on planar x-ray fluoroscopic images for lung and hepatic stereotactic body radiation therapy. Comparison to inhale/exhale CT technique *J. Appl. Clin. Med. Phys.* **21** 56–64

Shin D, Kang S, Kim K, Kim T, Kim D, Chung J, Lucero S A, Suh T S and Yamamoto T 2020 Development of a deformable lung phantom with 3D-printed flexible airways *Med. Phys.* **47** 898–908

Siemens Healthineers 2019 CT SOMATOM confidence brochure (available at: https://cdn0.scrvt.com/39b415fb07de4d9656c7b516d8e2d907/1800000006849454/d858e59aa190/siemens_healthineers_CT_SOMATOM_Confidence_Brochure_update_1800000006849454.pdf)

Singh V P and Badiger N M 2014 Effective atomic numbers of some tissue substitutes by different methods: a comparative study *J. Med. Phys.* **39** 24–31

Solc J, Vrba T and Burianova L 2018 Tissue-equivalence of 3D-printed plastics for medical phantoms in radiology *J. Instrum.* **13** P09018

Subramanian S V, Subramani V, Swamy S T, Gandhi A, Chilukuri S and Kathirvel M 2015 Is 5 mm MMLC suitable for VMAT-based lung SBRT? A dosimetric comparison with 2.5 mm HDMLC using RTOG-0813 treatment planning criteria for both conventional and high-dose flattening filter-free photon beams *J. Appl. Clin. Med. Phys.* **16** 112–24

Tanyi J A, Fuss M, Varchena V, Lancaster J L and Salter B J 2007 Phantom investigation of 3D motion-dependent volume aliasing during CT simulation for radiation therapy planning *Radiat. Oncol.* **2** 10

Tao Y, Kong F, Li Z, Zhang J, Zhao X, Yin Q, Xing D and Li P 2021 A review on voids of 3D printed parts by fused filament fabrication *J. Mater. Res. Technol.* **15** 4860–79

Tino R B, Yeo A U, Brandt M, Leary M and Kron T 2022 A customizable anthropomorphic phantom for dosimetric verification of 3D-printed lung, tissue, and bone density materials *Med. Phys.* **49** 52–69

Tino R, Leary M, Yeo A, Brandt M and Kron T 2019 Gyroid structures for 3D-printed heterogeneous radiotherapy phantoms *Phys. Med. Biol.* **64** 21NT05

Van Der Walt S, Schönberger J L, Nunez-Iglesias J, Boulogne F, Warner J D, Yager N, Gouillart E and Yu T 2014 scikit-image: image processing in Python *PeerJ* **2** e453

Virtanen P *et al* 2020 SciPy 1.0: fundamental algorithms for scientific computing in Python *Nat. Methods* **17** 261–72

White D R, Booz J, Griffith R V, Spokas J J and Wilson I J 1989 Report 44 *J. Int. Commun. Radiat. Units Meas.* **os23** NP